Chapter 1

Theory

This chapter outlines the theoretical basis for both the concepts and measurements relevant to this thesis. We start with very brief overview of Fermi liquid theory, leading on to the theory behind the de Haas–van Alphen (dHvA) torque technique, then a brief overview of density functional theory (DFT) and magnetotransport.

1.1 Fermi liquid theory

The nearly-free electron gas model for ordinary metals[*] is an extremely coarse approximation to the real situation and yet provides surprisingly good, predictive results in a variety of scenarios. Fermi liquid theory provides the theoretical basis which explains why we can use non-interacting particle models with a simple modification of the masses of the interacting Fermionic particles.

From a mathematical standpoint, Fermi liquid theory considers a gas of non-interacting particles and gradually 'switches on' the interactions. Provided the system transitions adiabatically[†] then the 'particles' in the resulting system, which is known as a *Fermi liquid*, can be modelled using the same mathematics as the non-interacting system with an adjusted mass. This adjusted mass is known as the *enhanced mass* and encompasses the interactions in the system with the magnitude being an indicator of the interaction strength. The enhanced mass particles are labelled quasiparticles since they no longer share the same mass as an electron at rest and are, arguably, a product of a mathematical abstraction.

At the time of writing, Fermi liquid theory describes what would be considered 'ordinary' metals with deviations from Fermi liquid theory generally considered of interest in a number of systems. Moreover the theory behind measurement techniques such as dHvA — described in the next section — rely on the existence of coherent quasiparticles at the Fermi surface to be valid. The reconciliation of observed dHvA oscillations in cuprates with evidence for reduced quasiparticle weight from angle resolved photoemission spectroscopy (ARPES) data currently provides one of the interesting challenges of high-T_c research.

---

[*]A model which only considers the kinetic energies of the electrons and Pauli exclusion terms

[†]i.e. with no symmetry breaking changes in phase or, in other words, there is a one-to-one mapping of the particles in the initial non-interacting system to the quasiparticles in the final interacting system

1.2   De Haas-va Alphen oscillation

In this section the phenomenon of dHvA oscillations is described. It is not immediately apparent how a ramping magnetic field could cause oscillations in such a wide range of parameters but Lifshitz and Kosevich provided an explanation through their eponymous equation based on a theoretical basis set out by Landau. This was then used to characterise the Fermi surface of many metals and establish the field of 'Fermiology'. Strictly, only the oscillations in magnetisation are dHvA oscillations and those in resistance are called Shubnikov-de Haas oscillations. Nonetheless they both originate from the same underlying phenomena of oscillations in the free energy of the system.

1.2.1   Overview

For metals, the majority of the interesting physics occurs at the Fermi level and, provided Fermi liquid theory holds true, the electrons at the Fermi level can be modelled to a high degree of accuracy with the Sommerfeld model — that is a Fermi gas of non-interacting electrons in an infinite box. When a magnetic field is applied, the electrons have their usual grid pattern distribution of plane wave k-vectors rearranged such that the electrons move around orbital and helical paths. These rearranged k-vectors form a set of concentric tubes, known as Landau tubes, whose cross-sectional area, a, perpendicular to the field is given by the Onsager relation:[*]

$$a_{k_\perp} = (r + 1/2)\frac{2\pi eB}{\hbar} \tag{1.2.1}$$

where r is a quantisation number that sets apart each tube. We can see from the relation that as $\boldsymbol{B}$ increases, so does the cross-sectional area of the tubes. As the magnetic field is ramped, successive tubes periodically pass the Fermi surface causing a spike in the density of states (DOS) at the Fermi level and also oscillations in the energy of the system, E, which, for geometric reasons explained in the next section, are far stronger at the maximal and minimal (extremal) areas of Fermi surface. Thermodynamic quantities such as magnetisation ($M = \partial E/\partial B$) and heat capacity ($C_V = \partial E/\partial T|_V$) or quantities that depend on the DOS at the Fermi level such as electrical resistance all oscillate as the field is ramped. Oscillations in the susceptibility are known as dHvA oscillations, oscillations in the resistivity are known as Shubnikov-de Haas oscillations.

We can relate the 'frequency' F (measured in $Tesla$[†]) that the tubes pass the Fermi surface to the extremal Fermi surface area using the following application of the Onsager

---

[*]Derivations of the Onsager relation are given in several textbooks including pg. 32 of Schoenberg [**Schoenberg1984**] and pg. 272 of Ashcroft & Mermin [**Ashcroft1976**].

[†]n.b. that it is $Tesla$ and not $Tesla^{-1}$ because, as we shall see later, the oscillations are actually periodic in $1/B$ and *not* B so their frequency counterpart is measured in $Tesla$.

relation,

$$a_{k_\perp} = \frac{2\pi e}{\hbar} F \tag{1.2.2}$$

By varying the direction of the field we can obtain a series of maximal and minimal Fermi surface areas in a variety of orientations in order to build a profile of the Fermi surface topology and size. In practice, there are many possible variations that might fit the model based on areas of cross-sectional slices alone and so typically ab-initio DFT calculations — described in sections 1.3 and **??** — are employed to provide a basis which can be tweaked based on the constraints from the measurements.

A more detailed analysis of this process follows, beginning with an illustrative mathematical treatment for oscillations in the magnetisation.

1.2.2 Exploring the origin of the oscillations

We begin by calculating the degeneracy of the Landau tubes i.e. the number of electron states per tube. Because the states under a magnetic field are a one-to-one rearrangement of the states with no field, we can use the Sommerfeld number of states per unit k-space $(V/4\pi^3)$ to determine the degeneracy. From the Onsager relation (eqn. 1.2.1) we see that the additional area for successive tubes is $\Delta a_{k_\perp} = 2\pi e B/\hbar$ which we can convert to a volume by integrating over $k_\perp$. This gives a degeneracy per tube therefore of,

$$D_{\text{tube}} = dk_\perp \left(\frac{2\pi e B}{\hbar}\right)\left(\frac{V}{4\pi^3}\right) = \frac{eBV dk_\perp}{\hbar 2\pi^2} \tag{1.2.3}$$

We continue by writing an expression for the energy of the system, E by summing the energies of the states that lie beneath the cross-sectional area defined by the Fermi surface $(a_{k_\perp F})$ for a given $k_\perp$. To do this, we use the Onsager equation to determine $R_\perp$ — the number of Landau tubes below the Fermi surface at this cross-sectional slice. We then multiply this by the degeneracy of the tubes, D and the energy for states on that particular Landau tube, ϵ_r,

$$E = D \sum_r^{R_\perp} \epsilon_r = \frac{eBV dk_\perp}{\hbar 2\pi^2} \sum_r^{R_\perp} \epsilon_r \tag{1.2.4}$$

where,

$$R_\perp = \text{floor}\left[\frac{a_{k_\perp F}\hbar}{2\pi e B} - \frac{1}{2}\right] \tag{1.2.5}$$

To complete the above equation, we need an expression for the energies of each of the Landau tubes. The procedure for the free electron case is to insert the canonical momentum (i.e momentum of a free electron in a magnetic field) into the non-interacting Schrödinger equation and solve to obtain the following eigenvalues for the energies on the Landau

tubes. Full derivations can be found in several textbooks[*] and so will not be repeated here. Below is the expression for the energy eigenvalues,

$$\epsilon_r = (r + 1/2)\hbar\omega_c + \frac{\hbar^2 k^2}{2m_0} \text{ where, } \omega_c = \frac{eB}{m_0} \tag{1.2.6}$$

and is known as the *cyclotron frequency*. The summation term in equation 1.2.4 can now be written,

$$\sum_r^{R_\perp} \epsilon_r = \sum_r^{R_\perp} \left((r + 1/2)\hbar\omega_c + \frac{\hbar^2 k^2}{2m_0} \right)$$

$$= \frac{\hbar eB}{m_0} \sum_r^{R_\perp} r + \frac{\hbar eB}{2m_0} \sum_r^{R_\perp} 1 + \frac{\hbar^2 k^2}{2m_0} \sum_r^{R_\perp} 1$$

$$= \frac{\hbar eB}{2m_0} R_\perp (R_\perp + 1) + \frac{\hbar eB}{2m_0} R_\perp + \frac{\hbar^2 k^2}{2m_0} R_\perp$$

$$= \frac{\hbar eB}{2m_0} R_\perp^2 + \left(\frac{\hbar eB}{m_0} + \frac{\hbar^2 k^2}{2m_0} \right) R_\perp$$

which can be expanded out and finally substituted back into equation 1.2.4 to finally obtain,

$$E = \frac{e^2 V \, dk_\perp}{4\pi^2 m_0} B^2 \left[R_\perp^2 + 2R_\perp + \frac{\hbar k^2}{e} \frac{1}{B} R_\perp \right] \tag{1.2.7}$$

Key to the above relation is that, although $R_\perp$ is inversely proportional to B, it remains discrete. This gives rise to the saw-tooth like function shown in figure 1.2.1 for some typical experimental parameters. Also plotted is the function against $1/B$ where we can clearly see that the oscillations are periodic in inverse field hence the frequency being measured in Tesla^{-1}.

The above is not a rigorous derivation but is nonetheless illustrative of the origin of the oscillation in the system energy and how any thermodynamic value which depends on the energy of the system oscillates as a function of field. To continue we need to include correction factors to the oscillation amplitude due to finite electron scattering rates (A_D), temperature (A_T), Zeeman splitting of spins (A_s), doping (A_{dop}), mosaicity (A_{mos}), warping of the Fermi surface (A_{warp}) as well as adjustments due to the fact that the parameter measured was torque of the sample in a field and not the energy or magnetisation directly (A_Γ). For this, we turn to a more solid foundation that was put forward by Lifschitz and Kosevitch.

---

[*]See for examples pg. 32ff. in Schoenberg [**Schoenberg1984**] or pg. 148ff. in Blundell [3].
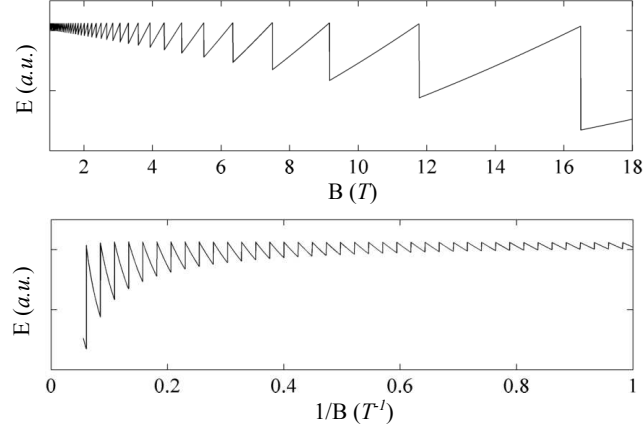
Figure 1.2.1: Theoretical energy oscillations for a Fermi surface orbit which is 5% of a 5 Å cubic BZ between 1-18 T. Kinetic energy term is taken to be for an electron at a level half the size of the Fermi surface.

1.2.3   Lifschitz–Kosevitch equation

The derivation for the full expression for the Landau thermodynamic potential, Ω^*, begins in a similar way to the previous illustrative example but frames the sawtooth-like function above as a more mathematically manageable Fourier decomposition which also conveniently makes the technique highly amenable to Fourier analysis. For this reason the equation below features higher harmonics which are denoted with the identifier p.

$$\Omega = \left(\frac{e}{2\pi\hbar}\right)^{\frac{3}{2}} \frac{e\hbar B^{\frac{5}{2}}}{m_0\pi^2} \left|\frac{\partial^2 a_{\text{ext}}}{\partial k_\perp^2}\right|^{-\frac{1}{2}} \sum_{p=1}^{\infty} p^{-\frac{5}{2}} A_{\text{tot}} \cos\left[2\pi p\left(\frac{F}{B}-\gamma\right)\pm\frac{\pi}{4}\right] \tag{1.2.8}$$

where,

$$A_{\text{tot}} = A_T A_D A_s A_\Gamma A_{\text{mos}} A_{\text{dop}} A_{\Delta B} \tag{1.2.9}$$

The above equation and derivatives of it are known as the Lifschitz–Kosevitch (LK) equation. To obtain the magnetisation the differential with respect to B is taken to get,

$$M = \left(\frac{e}{\hbar}\right)^{\frac{3}{2}} \frac{e\hbar FVB^{\frac{1}{2}}}{m_0\pi^{\frac{5}{2}}\sqrt{2}} \left|\frac{\partial^2 a_{\text{ext}}}{\partial k_\perp^2}\right|^{-\frac{1}{2}} \sum_{p=1}^{\infty} p^{-\frac{3}{2}} A_{\text{tot}} \sin\left[2\pi p\left(\frac{F}{B}-\gamma\right)\pm\frac{\pi}{4}\right] \tag{1.2.10}$$

To attain the above equations, it was necessary to perform an integral over $k_\perp$[†] which results in a parameter for an extremal Fermi surface orbit area perpendicular to the field given by a_{ext}.

---

[*]Formally defined as the energy in a open system that is in thermal contact with its surroundings
[†]Similar to the integral in the toy equation from the previous section

Attenuation for non-extremal orbits

Quantum oscillation measurement is often described as a probe of the extremal (i.e. the largest and smallest) Fermi surface orbits perpendicular to the magnetic field. However it is not immediately clear how this comes about, nor how some hypothetical Fermi surfaces, such as a perfect cone, would appear in quantum oscillation measurements.

Strictly, all cross-sectional orbits along $k_\perp$ contribute to the system energy as determined in the LK equation and each of these orbits has a particular frequency, $F(k_\perp)$, related to its orbital area by eqn. 1.2.2. Since all these frequencies interfere, the regions of $k_\perp$ where the frequencies vary the least dominate the contribution to the system energy, i.e. where $dF(k_\perp)/dk_\perp$ is smallest. In other words, regions along $K_\perp$ where there are stationary points in $F(k_\perp)$ contribute the most to the oscillations in the system energy.

This means for a hypothetical conical Fermi surface with sharp edges, for a field along the cone axis, there would be no stationary points in $F(k_\perp)$ and there would be no dominant frequency contributing to the oscillations in the system energy *from stationary points*. However it may be possible that a conical Fermi surface can contribute a signal to the Fermi surface that is comparable to a stationary point if the wide end of the conical Fermi surface is comparable in size to the momentum spacing of the Landau tubes. This restricts the field regimes in which oscillations can occur.

The above is illustrated in figure 1.2.2. The insets shows a cross-sectional slice of the described hypothetical conical Fermi surface as the dashed lines, and a parabolic Fermi surface as a solid line. Assuming field is applied along k_z, the parabolic Fermi surface has a stationary point at its midpoint, the conical Fermi surface has no stationary points. The main panels each show the result of numerically integrating $\int \cos{(2\pi F(k_\perp/B)dk_\perp}$ where $F(k_\perp)$ is related to the cross-sectional area of Fermi surfaces in inset through eqn. 1.2.2. The maximum radii of the hypothetical Fermi surfaces increase in each panel from $k_r = 0.0075\,\text{Å}^{-1}$ in the top left panel to $k_r = 0.05\,\text{Å}^{-1}$ in the bottom right.

For the cases where the sides of the conical surface are steep, then the associated oscillation is weaker than that from the comparable parabolic Fermi surface as is shown in the bottom two panels of figure 1.2.2. However, for the narrow Fermi surfaces, the top two panels show how above a particular field, where the spacing between successive Landau tubes become large in momentum, the signal from the conical and the parabolic surface become comparable. This makes sense if we consider the Landau tubes as an oscillatory probe — the resolution is limited by wavelength and in this regime the relatively flat conical sides cannot be distinguished from a stationary point.

To measure the finer stationary point features on the Fermi surface (i.e. shallow corrugations or small pockets) attention needs to be paid to the rapidly oscillating low field region. As can be seen in the top two panels, the parabolic signal is much stronger than the conical signal here. However this region is often obscured by technical problems of high frequency Johnson noise, insufficient sample rates and superconductivity.
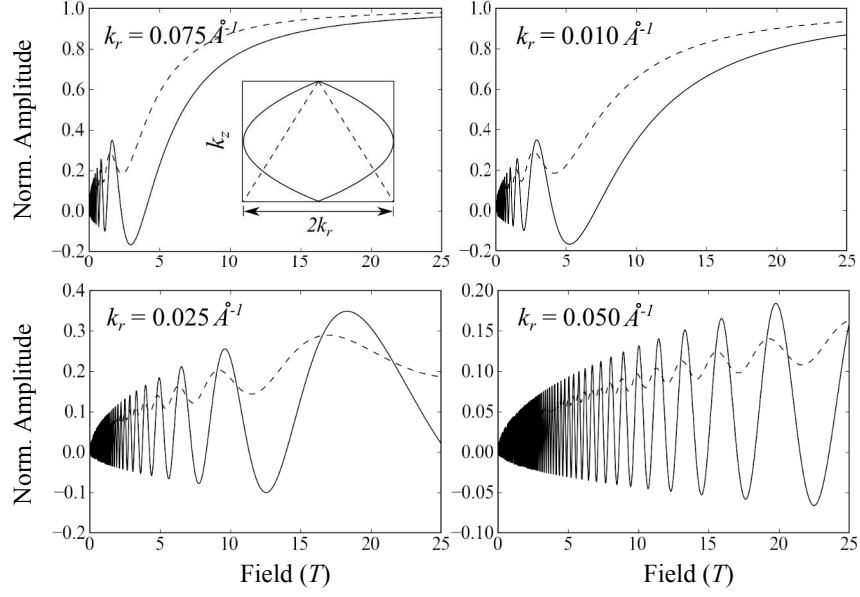
Figure 1.2.2: Inset: hypothetical radially symmetric Fermi surface slices in the [110] plane with maximum radius k_r shown: dashed line is conical, solid line is parabolic. Main panels: Results of $\int \cos(2\pi F(k_\perp)/B)dk_\perp$ where $F(k_\perp)$ is related to the cross-sectional area of Fermi surfaces in inset through eqn. 1.2.2, from top left: $k_r = 0.075, 0.01, 0.025, 0.05$ respectively.

The data analysis also requires sufficient oscillations for an fast fourier transform (FFT). The top right panel of figure 1.2.2 shows that in the region of 6 T and above, only half an oscillation has occurred meaning FFT is unlikely to give a strong signal. Since data in the dHvA experiment was taken between 6 T and 18 T we should not expect to be able to resolve pockets of radius less than $k_r \sim 0.01\,\text{Å}^{-1}$.

We move now to the other attenuating factors listed towards the end of section 1.2.2. The above calculation demonstrated how a distribution of frequencies can attenuate an oscillation. At infinity, interfering oscillations with a distribution of frequencies can be approximated instead as interfering oscillations with a distribution of phases. Because the oscillations we are measuring are in inverse field, once they become resolvable due to the experimental problems of noise, sample rates etc. the infinite oscillation approximation becomes valid. This means we can model each attenuating factor by convolving an appropriate phase distribution function with the cosine oscillatory term. It can be shown[*] that this convolution results in a relatively simple multiplication factor — hence the various A factors listed in the LK equation which we expand upon below.

---

[*]See for example, Schoenberg pg 57–59. [**Schoenberg1984**]

Attenuation due to temperature

To find the appropriate phase distribution function for the temperature dependence we start with the Fermi distribution,

$$f(\epsilon) = \frac{1}{\exp\left((\epsilon - \mu)/kT\right) + 1} \tag{1.2.11}$$

The differential of this distribution results in the broadening function (which is proportional to the probability that the Fermi energy μ is between ϵ and $\epsilon + d\epsilon$),

$$P(\epsilon < \mu < \epsilon + d\epsilon) \propto \frac{d\epsilon}{2kT(1 + \cosh[(\epsilon - \mu)/kT])} \tag{1.2.12}$$

This is convolved with the energy distribution which smears the Fermi surface. Because the Fermi surface is smeared, so is the parameter F which spreads the Fourier transform peak due to the oscillation in the system energy, leading to an attenuation of the Fourier amplitude. The final attenuation factor due to this smearing is given in Schoenberg pg. 59ff [**Schoenberg1984**] and is reproduced below,

$$A_T = \frac{X}{\sinh(X)} \quad \text{where,} \quad X = \frac{2\pi^2 pkTm_T^*}{e\hbar B} \tag{1.2.13}$$

The above factor includes m_T^*, the *thermal effective mass* as a term in a function of T. As a consequence, by studying the temperature dependence of the amplitude it is possible to get a measure of m_T^* of the electrons at the extremal orbit. Techniques for doing this are discussed in section **??**.

The LK equation arises from a semi-classical approach in that it considers a system of single particle Bloch functions which are manipulated using classical relations. Many-body effects such as electron-phonon and electron-electron interactions were incorporated later in the development of quantum oscillation theory and were shown to affect A_s and A_T. In the above case, A_T is modified by both electron-phonon and electron-electron effects which is manifest through changes to the effective mass term [**Schoenberg1984**]. The effective mass determined in this way is enhanced subject to the same interactions as in heat capacity experiments but are probed for a particular Fermi surface orbit, whereas heat capacity is averaged over the entire Fermi surface. As we will see later the thermal mass enhancement is is different to the mass enhancement from spin measurements. For more one this see Rourke *et al.* [**Rourke2010b**], [**Schoenberg1984**] and references therein.

Attenuation due to finite quasiparticle lifetime

The *Dingle factor*, A_D, is due to the finite lifetime, τ, of the electron quasiparticles due to scattering. Because of this time scale, there is a smearing of the electron energy through

the uncertainty principle with a broadening which is approximately Lorentzian in shape. If we assume τ does not change with energy*, then this can be modelled as a smearing of the Fermi level such that the broadening function is,

$$P(\epsilon < \mu < \epsilon + d\epsilon) \propto \frac{d\epsilon}{(\epsilon - \mu)^2 + (\hbar/2\tau)^2} \tag{1.2.14}$$

and such that after the routine Fourier transform, the end relation is given by,

$$A_D = e^{-\pi p m_b/eB\tau} = e^{-\pi p/\omega_c \tau} \tag{1.2.15}$$

The exponent in the above can be thought of as the number of orbits the electron has completed (i.e. each harmonic p is another successive orbit) divided by the expected number of orbits it will complete, so evidently we expect to see the higher harmonics having an exponentially lower amplitude. The term m_b refers to the *band mass* which will be discussed in detail later on. Sometimes when discussing the Dingle term, we refer to the Dingle factor which is the factor in the exponential defined as $\alpha \equiv -\pi p m_b/(e\tau)$.

Attenuation due to spin splitting

Applying a magnetic field causes a Zeeman splitting of energy levels of magnitude,

$$\Delta\epsilon = \frac{g\mu_B B}{2} \tag{1.2.16}$$

where μ_B is the single electron magnetic moment (the Bohr magneton) and g is a factor that is ≈ 2 for free electrons. Rather than smearing, this can be thought of as two separate Fermi surfaces with separate Fermi energies. The attenuation is given now as,

$$A_s = \cos\left(\frac{\pi p g m_s^*}{2}\right) \tag{1.2.17}$$

where m_s^* is the *spin effective mass*. This is subject to a different set of many-body interactions in comparison to the thermal effective mass – notably only electron-electron correlations and not the electron-phonon interactions. Moreover, whilst the spin effective mass is affected by the many body effects, so is the Landau g factor and even the shape of the Fermi surface. The spin mass enhancement is related to the standard Stoner enhancement factor, $S = 1/(1 - IN(E_F))$ by $m_s^* = (1 + S)m_b$.

---

*This is not the case, but at most only a few Landau levels contribute to a particular oscillation and if we assume that the energy does not vary too much between subsequent levels then the assumption is a good one

Other attenuating factors

Another attenuating factor due to slight misalignments in the crystal structure, (A_{mos}), causing a mosaic polycrystalline structure that can be modelled with an appropriate broadening function. Schoenberg suggests a Lorentzian broadening function, which leads to an attentuation term which is similar to 1.2.15, although the actual distribution of misalignments could be any distribution. Given a Lorentzian broadening function, the final form would look like the following,

$$A_{\text{mos}} = e^{2\pi p \Delta F_{\text{mos}}/B} \tag{1.2.18}$$

where ΔF_{mos} is a parameter that determines the degree of overall misalignment.

The final attenuating factors mentioned here are $A_{\Delta B}$, the damping due to field inhomogeneity which has an effect depending on the shape of the field and A_{dop}, which is another Lorentzian-like broadening factor due to the doping inhomogeneity in the sample. Neither of which will be considered in the thesis — the material studied is undoped, and the magnet is suitably large as to have an essentially constant field profile — and so will not be explored further[*]

1.2.4 Band mass

So far, three different electron masses have been defined, the thermal effective mass, the spin effective mass and the free electron mass. To tie these together a fourth mass is introduced, the *band mass*. This is another effective mass resulting from the electrons being subject to the bandstructure potential as defined by DFT calculations and is given by,

$$m_b^* = \frac{\hbar}{2\pi} \oint_{\text{Orbit}} \frac{d\boldsymbol{k}}{v_F(\boldsymbol{k})} = \frac{\hbar^2}{2\pi} \frac{\partial a_{k_\perp}}{\partial \epsilon} \tag{1.2.19}$$

Mass enhancement comes from any kind of interactions the electron has with its environment — i.e. external fields, other electrons and nuclei — resulting in the free electron mass m_e becoming enhanced (renormalised). The band mass can be determined from DFT and the resulting enhancement results from the mean-field effects of the DFT calculation as reflected in the calculated band structure. However DFT calculations typically do not model correlation effects well or dynamic interactions at all. We know that both the thermal effective mass and the spin effective mass incorporate the band mass enhancements plus a unique set of interactions specified previously. Figure 1.2.3 lays out how the effective masses build on each other by incorporating more interactions. because of this particular hierarchy, it is sometimes possible to compare effective masses to get a sense of scale of the interactions.

---

[*]If you do want to consider these factors, ref [**Rourke2010b**] has a passage on doping homogeneity and pg. 64 of Schoenberg discusses field inhomogeneity **??**.
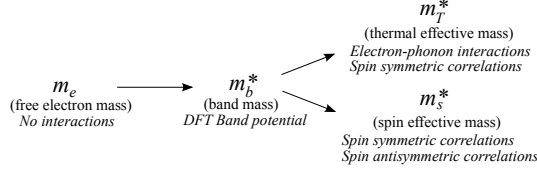
Figure 1.2.3: A diagram showing how the successive electron masses build on the previous interactions. Additional interaction effects are listed in italics.

A 2D Approximation

Although none of the attenuating factors above have an explicit angle dependence, they do vary as a function of angle through the band mass. A common approximation to simulate the dependency in layered systems is to assume the Fermi surface is two dimensional in shape and therefore cylindrical. The cross sectional area of a cylinder is given by,

$$a = \frac{a_0}{\cos\theta},$$

(1.2.20)

where θ is the angle from the cylinder axis. Increasing the Fermi energy by $\Delta\epsilon$ will cause the cross section at zero angle to change by amount Δa_0, then the band mass is given by,

$$m_b^* = \frac{\hbar^2}{2\pi}\frac{\partial a_{k_\perp}}{\partial\epsilon} = \frac{\hbar^2}{2\pi}\frac{\partial}{\partial\epsilon}\left(\frac{a_0 + \Delta a_0}{\cos\theta} - \frac{a_0}{\cos\theta}\right) = \frac{\hbar^2}{2\pi}\frac{\partial a_0}{\partial\epsilon}\frac{1}{\cos\theta},$$

(1.2.21)

therefore

$$m_b^* = \frac{m_{b0}^*}{\cos\theta}$$

(1.2.22)

This means that under this approximation, any factor that includes the band mass, explicitly or implicitly* can be resolved using the zero angle band mass with an angle dependence of $1/\cos\theta$.

1.2.5 Final theoretical observations

Originally dHvA measurements were used to measure the Fermi surfaces of elemental metals and so the initial assumption of a free-electron gas is justified based on the fact that elemental metals have a Fermi surface and are considered materials that adhere to Fermi liquid theory. The fact that oscillations have been observed in cuprates and pnictides which have demonstrated non-Fermi liquid behaviour is therefore remarkable and moreover implies the presence of a Fermi surface, at least in the presence of a strong magnetic field. States in which these conditions co-incide are usually referred to as 'generalised Fermi liquids' which demonstrates some of the hallmarks of Fermi liquid such as a Fermi surface but not others such as an energy squared dependence of the imaginary self energy. For

---

*Meaning m_T^* and m_S^* which are both enhancements of the band mass

more details see refs. [**Wasserman1991**] and [**Wasserman1996**].

1.3 Spin density wave instability

Section **??** discussed the possibility of high-T_c pairing being due to fluctuations in close proximity to a spin density wave (SDW) state. Here we briefly describe the SDW state and some of the theory behind it.

Broadly speaking a SDW is a magnetic state just as ferromagnetism and antiferromagnetism are magnetic states. In its most general sense, a SDW is a periodic modulation of magnetic spins in both space and time hence it being a 'wave of spin density'. atomic force microscope (AFM) is actually a special case of a SDW which does not vary in time, i.e. is static, and also varies spatially with the periodicity being some multiple of the real-space lattice vector, i.e. is commensurate with the lattice. Ferromagnetism can be thought of as a SDW state with wavevector $\boldsymbol{q} = 0$ i.e. it has no periodic variation and so is not really a 'wave'.

Using the mean field Hartree-Fock approximation (HFA) the following expression gives the stability condition for the SDW state [**Moriya1985**],

$$2I\chi_0(\boldsymbol{q}) > 1, \tag{1.3.1}$$

where I is the exchange energy between electron bands and χ_0 is the Lindhard susceptibility. The greater the Lindhard susceptibility, the more stable the state.

1.3.1 Lindhard susceptibility

The Lindhard susceptibility models the Stoner excitations (i.e. electron-hole scattering) of a nearly free electron system. To derive the Lindhard susceptibility, we begin with a Fermi liquid i.e. a Pauli excluded but otherwise non-interacting gas of free electrons. We calculate* the first order perturbative linear response of this gas to to a magnetic field given by $\boldsymbol{B} = \exp(\boldsymbol{q.r} - \omega.t)$. The resulting equation is often quoted as,

$$\chi_0(q,\omega) = \lim_{\delta \to 0} \sum_k \sum_{l,l'} \frac{f(\epsilon_{k+q,l'}) - f(\epsilon_{k,l})}{\epsilon_{k+q,l'} - \epsilon_{k,l} - \hbar\omega - i\delta} D \tag{1.3.2}$$

where,

$$D = |\langle k+q, l'|V|k,l\rangle|^2 \tag{1.3.3}$$

and is the matrix transition element for the scattering process. The numerator term contains two Fermi functions — the same as eqn. 1.2.11 — which ensure that the susceptibility is finite for states which scatter across the Fermi energy and zero if they do not - conse-

---

*Not presented here but pg 81 ff. of Dressel [2] has a full derivation.

quently, the Lindhard susceptibility models electron-hole scattering (Stoner excitations) in particular. The Fermi functions also smear the susceptibility dispersion as a function of temperature. The third term in the denominator corresponds to the excitation energy of the perturbing field with ω corresponding to the temporal frequency of the field. The final term in the denominator is an artefact of the adiabatic approximation used to calculate the perturbation with the completed approximation taking the limit of $\delta \to 0$. The first sum in the Lindhard function is over all k states in the first BZ, the second sum combines each energy band. The real and imaginary parts of equation 1.4.2 are,

$$\text{Re}\{\chi_0(q,\omega)\} = \lim_{\delta \to 0} \sum_k \sum_{l,l'} \frac{(\epsilon_{k+q,l'} - \epsilon_{k,l} - \hbar\omega)(f(\epsilon_{k+q,l'}) - f(\epsilon_{k,l}))}{(\epsilon_{k+q,l'} - \epsilon_{k,l} - \hbar\omega)^2 + \delta^2} D \qquad (1.3.4)$$

$$\text{Im}\{\chi_0(q,\omega)\} = \lim_{\delta \to 0} \sum_k \sum_{l,l'} \frac{-\delta(f(\epsilon_{k+q,l'}) - f(\epsilon_{k,l}))}{(\epsilon_{k+q,l'} - \epsilon_{k,l} - \hbar\omega)^2 + \delta^2} D \qquad (1.3.5)$$

$$(1.3.6)$$

respectively. The real part is important in the context of instabilities in metals, the imaginary part gives the resonance modes for bosonic excitations of energy $\hbar\omega^*$.

The Lindhard function is a simple linear response for a particular static charge configuration. As soon as the charge configuration shifts due to the perturbing field the potential changes and so does the response. To compensate we consider the perturbing field to be adjusted by considering an additional induced field due to the changing charge along with the perturbing field and calculate the linear response in terms of that new combined field. This new form is the *first renormalisation*. This is still not perfect however since now the charge density changes again in a different way due to this new combined potential and so a second induced potential has to be considered giving the *second renormalisation* and so-on. This process of renormalisation forms the basis of linear response theory. In practice the random phase approximation (RPA)* is generally invoked where corrections beyond the first renormalisation are ignored. The RPA response of the Lindhard susceptibility is as follows,

$$\chi(\boldsymbol{q},\omega) = \frac{\chi_0(\boldsymbol{q},\omega)}{1 - \frac{4\pi e^2}{q^2}\chi_0(\boldsymbol{q},\omega)} \qquad (1.3.7)$$

Peaks in this function correspond to scattering of states which cross the Fermi energy yet remain close to the Fermi energy. We can derive this function by modelling an oscillatory perturbing field on a system. To solve to get an expression for the second order perturbation, we make the adiabatic limit approximation (i.e. the perturbing potential is gradually increase from zero at $t = \infty$ to v at $t = 0$).

Although knowledge of the susceptibility is useful to model, for example, neutron

---

*e.g. plasmons, spin density waves, charge density waves, phonons etc.

*So called because it is considered that the charge densities in the higher renormalisations are from electron wavefunctions which have randomly shifted phases and so cancel each other out.

scattering measurements, for our purposes we will use it as an indicator of possible SDW instability vectors in our example materials. For this reason we make the assumption that the transition matrix elements are unity. This assumption greatly simplifies the calculations at the cost of some structure and as such should be borne in mind that the results are somewhat broad and qualitative.

1.3.2   Notes on practical calculation

Taking the limits of $\delta \to 0$ of eqn. 1.4.6 which is effectively an ever narrowing Lorentzian distribution, results in an expression for the imaginary part of Lindhard susceptibility, $\mathrm{Im}(\chi_0) \propto \delta(\epsilon_{k+q,l'} - \epsilon k, l - \hbar\omega)$ where δ here is the Dirac delta function. In a calculation on a continuous energy dispersion, this results in resonances at excitations which match the difference in energies between states. However, in this thesis, the energy dispersions used to determine nesting conditions are not continuous and instead are based on discrete energies obtained from DFT calculations. As such δ will have to remain finite in order to broaden the delta function into a Lorentzian with width comparable to the energy differences between the discrete points – the net result of this will be loss of some fine structure.

Secondly, only bands that lie close to the Fermi energy contribute significantly to the susceptibility. Since the calculations are computationally costly, only bands which are close (within the adiabatic or temperature broadening) to the Fermi energy are input into the calculations.

1.4   Density functional theory

The interpretation of the dHvA measurements presented later in this thesis rely to some extent on the ab-initio calculation of the energy bands of $BaFe_2P_2$ using the WIEN2k code [**Blaha2001**] — the technique used to find these energy dispersions are based on a DFT scheme. The following is broad overview of DFT which is drawn from notes from a series of summer school lectures by M. Lüders [**Luders2010**] and the 'ABC of DFT' by K. Burke [**Burke2003**].

Although implementations of DFT rely on various approximations, the theory of DFT itself has been shown to be exact and mathematically rigorous. It comprises of a set of theorems developed and proven by Hohenberg, Kohn and Levy [**Hohenberg1964**, **Levy1979**] and a methodology for solving to obtain the ground state energies developed by Kohn and Sham. The principle theorem outlined by Hohenberg-Kohn (HK) shows that the ground state external potential, $v_{\mathrm{ext}}(\boldsymbol{r})$, of a system can be determined by the ground state density, $n(\boldsymbol{r})$, alone and vice-versa. A second HK theorem outlines a minimisation

condition which expresses the ground state energy as follows,

$$\frac{\partial F[n]}{\partial n(\boldsymbol{r})} + v_{\text{ext}}(\boldsymbol{r}) = \mu, \tag{1.4.1}$$

where,

$$F[n] = T[n] + V_{\text{ee}}[n] \tag{1.4.2}$$

$F[n]$ is the 'universal' functional* and $T[n]$ and $V_{\text{ee}}[n]$ are the kinetic and correlation functionals respectively. μ is the chemical potential which is introduced as a normalisation term that ensures that there are an appropriate number of electrons in the charge density. The universal functional is so called because the system is completely defined in the external potential term alone and so $F[n]$ is common to all systems, nonetheless it still requires approximation. For this reason as well as the fact that there are no clues from the HK theorems as to a good starting form for n, still means the problem is intractable.

Kohn-Sham developed a method to find a good starting form for n by showing that there exists a pseudo-potential, v_{KS}, that satisfies the above equation for a *non-interacting* system, i.e. $F[n] = T[n]$, which shares the same n as the original interacting system. This abstract potential, which takes the place of v_{ext} in the above equation, has no strict physical meaning but it allows us to build a common expression for n in terms of a sum of single particle wavefunctions. It is given as follows,

$$v_{\text{KS}} = v_{\text{ext}}(\boldsymbol{r}) + \int d^3 r' \frac{n(\boldsymbol{r})}{|\boldsymbol{r} - \boldsymbol{r}'|} + \frac{\partial E_{\text{xc}}}{\partial n(\boldsymbol{r})} \tag{1.4.3}$$

where E_{xc} is the combined particle correlation and exchange energy terms which is approximated according to the type of problem to be solved*. Once an approximate form for the exchange term has been chosen, the above can be used to find the ground state energy by running a self consistency cycle that forms the heart of most DFT codes,

1. Guess an initial $n_{i=0}$

2. Calculate v_{KS} from n_i using eqn. 1.3.3

3. Minimise the non-interacting (Kohn-Sham) form of eqn. 1.3.1

4. Calculate the new n_{i+1}

5. Repeat from step 2 with n_i being adjusted by n_{i+1} until $n_i - n_{i+1} <$ some tolerance

---

*A functional maps a function onto a single vector or scalar — typically by integrating over the function — and is commonly denoted with the function parameter in square brackets. Compare this with the definition of a function which maps a series of scalars onto a single scalar or vector.

*Note that in principle, these two terms should be separate but most approximations tend to combine them into a single term.

Simply replacing n_i with n_{i+1} can cause the calculation to rapidly diverge and so instead a mixing scheme is used. Typically this incorporates a small fraction of n_{i+1} with the rest made up of the old n_i. A more complex mixing scheme can be employed to ensure more rapid convergence, the Broyden mixing scheme for example uses a Newton-Raphson style root finding mechanism on the Jacobian of the $n_i - n_{i+1}$ [**Broyden1965**].

1.4.1   The generalised gradient approximation

The correlation term represents the most significant approximation in the calculation of DFT. For the DFT presented in this thesis, the generalised gradient approximation (GGA) was used which is part of the family of local density approximations (LDAs). The simplest (i.e. lowest order) LDA takes the effects of the electron-electron correlations at point r to be constant throughout the system with the magnitude based on the charge density at r. This works particularly well for free-electron-like systems with lots of itinerant valence electrons since the electrons are evenly spread throughout — however it does not work so well for highly localised Hubbard-like systems where there is a high density of electrons at atomic sites, but very little density just off the sites. A step towards improving this comes by raising the order of the approximation so that it modifies the constant local density with the rate of change of the local density as you move off the site (i.e. the local charge density gradient). It turns out however that incorporating the gradient results in less accuracy than the simple LDA due to the LDA 'accidentally' cancelling a series of so called sum rules. The GGA builds on the higher order gradient approximation by incorporating the cancelling of the sum rules to obtain a reasonably accurate approximation to the correlation potential.

The precise way to express the GGA however is still a matter of debate though with there being multiple implementations [**Perdew1996**, **Perdew1986**], each of which may give slightly different results[†]. Nonetheless GGAs tends to perform better than zeroth order LDA with inhomogeneous electron densities.

1.4.2   Single particle wavefunction bases

Typically, close to the atom, electrons tends to have a radial symmetry whereas itinerant valence electrons are more planewave-like. Matching each of these to an appropriate single particle basis set dramatically reduces the amount of calculation time. The augmented plane wave (APW) method defines a series of 'muffin-tin spheres' which are centred on each of our atoms. Those well inside are described in terms of radial basis orbitals, those well outside are described in terms of plane waves.

Andersen further simplified the radial basis portion of the APW method by approximating the wavefunctions by a first order Taylor expansion with respect to en-

---

[†]See for example table 1 in ref. [**Perdew1996**]

ergy [**Andersen1975**]. The result is known as linearised augmented plane wave (LAPW).

1.4.3 Local orbit wavefunction bases

The standard LAPW method can be made more efficient by up to an order of magnitude if additional wavefunctions are included with the standard APW wavefunctions which better describe the states close to the edge of the muffin tin spheres known as the *semi-core states*.

These additional wavefunctions are known as *local orbitals* and allow the calculation to relax the condition that the standard APW wavefunctions must have a continuous slope at the muffin tin boundary. The local orbit wavefunctions are used to smooth over the kinks where the plane wavefunctions and the radial wavefunctions meet. The functions are radial in nature but are $\boldsymbol{k}$ independent. Including these wavefunctions can result in up to 50 % fewer wavefunctions required for convergence and significantly shorter calculation times [**Madsen2001**].

1.4.4 Code and execution details

Calculations presented in this thesis were performed using WIEN2k version 07.2 (20th Feb 2007) [**Blaha2001**] using LAPW without the local orbitals. Unless specified, non-spin orbit calculations are presented although spin-orbit calculations were checked and did not show significant differences. The GGA according to Perdew-Burke-Ernzerhof [**Perdew1996**] was used for the exchange correlation functional.

Preprocessing of the WIEN2k data into voxel form as well as the theoretical angle plots were performed using a modified version of MATLAB code written by Dr. E. Yelland. The basis for the code has been thoroughly field tested within the group over a number of years.

1.5 Hall effect

The Hall effect is a consequence of the Lorentz force on a moving charge. To first understand this we look to the Boltzmann transport equation which allows us to use a semi-classical approach to incorporate the effects of magnetic field to find expressions for single electron transport and in particular the conductivity tensor ρ. The Boltzmann transport equation is expressed as follows,

$$\frac{\partial f}{\partial t} + \boldsymbol{v}.\nabla_r f + \boldsymbol{F}.\nabla_k f = \left.\frac{df}{dt}\right|_{\text{coll}}, \tag{1.5.1}$$

where $f = f(\boldsymbol{r}, \boldsymbol{k}, t)$ is the occupation distribution for single electrons at position $\boldsymbol{r}$, in state $\boldsymbol{k}$ at time t and $\boldsymbol{v}$ is the electron velocity, $\boldsymbol{F}$ is the force on the electron and the term on the right is the rate of change of the occupation due to collisions. The Boltzmann

transport equation arises from the notion that, classically, the chance of occupation of a particular state f at t is equivalent to the probability of occupation of a state at $f - df/dt$ at time $t - dt$. The fact that the equation employs classical dynamics with quantum mechanical Bloch waveforms makes this a semi-classical equation.

The collision term on the right is generally complicated and is usually approximated by the *relaxation time approximation*,

$$\left. \frac{df}{dt} \right|_{\text{coll}} = \frac{f - f_0}{\tau}, \tag{1.5.2}$$

where f_0 is the equilibrium occupation distribution to which f tends towards exponentially if the system is perturbed. The rate of the exponential convergence is determined by the relaxation time, τ, with the decay rate of the discrepancy being proportional to $e^{-t/\tau}$.

As discussed in section 1.2.1, electrons at the Fermi surface subject to a magnetic field are confined to orbits of a particular area around the Fermi surface due to the Lorentz force. Dealing solely with the simpler case of closed orbits (c.f. open orbits), we make an approximation of a steady state and uniform distribution so the first two terms of eqn. 1.5.1 are zero. We then incorporate the Lorentz force, $\boldsymbol{F} = q(\boldsymbol{E} + \boldsymbol{V} \times \boldsymbol{B})$, in the third term. Finally through some manipulations [**French2009**] and on assuming that $k_b T \ll E_F$ so the Fermi distribution is a step function, then we can obtain an expression for the conductivity tensor elements, σ_{ij}, as the Shockley-Chambers tube integral form of the Boltzmann equation,

$$\sigma_{ij} = \frac{e^2}{4\pi^3 \hbar^2} \int \partial k_B \int_0^{2\pi} \partial\phi \int_0^\infty \partial\phi' v_i(\phi) v_j(\phi - \phi') \frac{m^*}{\omega_c} e^{\phi'/(\omega_c \tau)} \tag{1.5.3}$$

where ϕ and ϕ' are angular integration variables around the orbit. From this integral it is possible to determine the conductivity tensor for a variety of Fermi surface geometries, however given the shape of the $\text{Bi}_{2+z-y}\text{Pb}_y\text{Sr}_{2-x-z}\text{La}_x\text{CuO}_{6+\delta}$ (BSCO2201) Fermi surface, we are most interested in the cylindrical Fermi surface which gives the following conductivity tensor, ρ for a magnetic field applied along z,

$$\rho = \begin{pmatrix} \rho_{xx} & \rho_{xy} & \rho_{xz} \\ \rho_{yx} & \rho_{yy} & \rho_{yz} \\ \rho_{zx} & \rho_{zy} & \rho_{zz} \end{pmatrix} = \begin{pmatrix} 1/\sigma_0 & \omega_c\tau/\sigma_0 & 0 \\ \omega_c\tau/\sigma_0 & 1/\sigma_0 & 0 \\ 0 & 0 & 0 \end{pmatrix} \tag{1.5.4}$$

where ω_c is the cyclotron frequency and σ_0 is the Drude conductivity given by,

$$\sigma_0 = \frac{ne^2\tau}{m^*} \tag{1.5.5}$$

where n is the carrier density and m^* is the effective mass. The off-diagonal resistivity component represents the resistivity perpendicular to the current and in the case of $\rho_{xy}(=$

ρ_{yx}) is also perpendicular to the field then this is known as the Hall resistivity,

$$\rho_{xy} = \frac{\omega_c \tau}{\sigma_0} = \left(\frac{eB}{m^*}\right) \tau \frac{m^*}{ne^2 \tau} = \frac{B}{ne} \qquad (1.5.6)$$

The Hall resistivity can be understood if we consider an electron (hole) moving along a rectangular slab subject to a perpendicular magnetic field. The electrons (holes) are deflected to one side of the slab due to the Lorentz force on the charged particle. Eventually the charge density one one side becomes high enough that the Coulomb repulsion force of the density on subsequent charge carriers balances the Lorentz force and an equilibrium voltage between either side of the slab is reached. This voltage is known as the Hall voltage, V_H and is given by,

$$V_H = -\frac{I\rho_{xy}}{d} = -\frac{IB}{ned} \qquad (1.5.7)$$

where I and $B_\perp$ are the current and perpendicular magnetic field and n, e and d are the carrier density, charge and slab thickness respectively. V_H is what is measured in our experiment. This is usually further abstracted to the Hall coefficient, R_H, which encapsulates the carrier density for a metal as follows,

$$R_H = \frac{V_H d}{IB} = \frac{1}{ne} \qquad (1.5.8)$$

Provided the magnetic field is small, meaning $\omega_c \tau \ll 1$, then scattering prevents the formation of Landau tubes described in section 1.2.1. This is known as the low field limit. The high field limit leads to effects such as the quantum Hall effect and quantum oscillations.

1.5.1 Effects of Fermi surface topology

Ostensibly, a hole-like Fermi surface would be expected to demonstrate positive Hall coefficient and an electron-like Fermi surface a negative, however it is possible to obtain the exact opposite due to the curvature of the Fermi surface [**Narduzzo2008**].

For a 2D metal in the weak field semiclassical limit, Ong determined that the transverse conductivity, σ_{xy} from which R_H is derived can be obtained by integrating the mean free path vector, $l_k = v_k \tau_k$ over the Fermi surface (v_k is the Fermi velocity and τ_k is the momentum dependent scattering rate). This is illustrated in figure 1.5.1 which integrates over a Fermi surface with a long mean free path in the (π, π) direction and shows how the resulting l_k traces two loops in opposite directions giving rise to a larger 'negative' loop from the negative curvature even though the overall surface has a positive curvature. This illustrated scenario is close to what we find in the cuprates at high doping. Here the mean free path is affected by the anisotropic scattering rate detailed in the introduction section and the proximity of the van-Hove singularity leads to negative curvature in the long flat
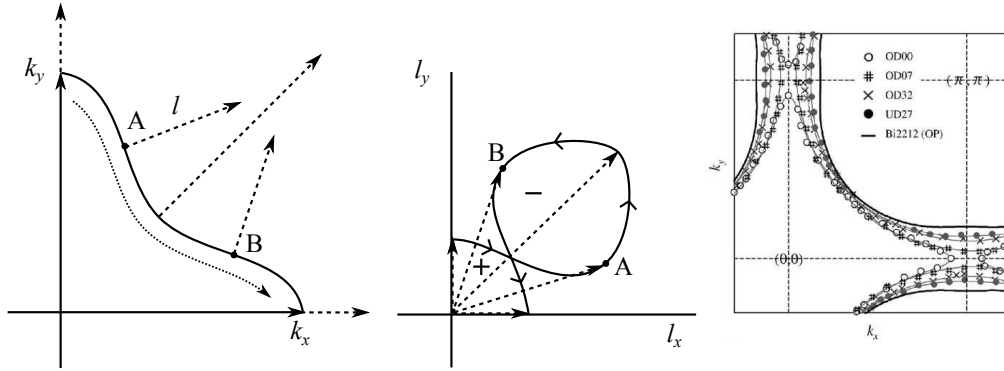
Figure 1.5.1: Left illustrates a negatively curved Fermi surface with a long mean free path along the $k = (\pi, \pi)$ portion and the integral progressing along the dotted line. Middle shows how the mean free path vector changes along the integral line tracing two loops of opposite direction. Adapted from ref. [**Narduzzo2008**]. Right shows the progression of the BSCO2201 Fermi surface about the van-Hove singularity. Adapted from ref. [**Kondo2004**].

sides of the Fermi surface as it changes between hole-like and electron-like, as shown for BSCO2201 in the right side panel of figure 1.5.1, adapted from ref [**Kondo2004**].